



Ligand Control of Low-Frequency Electron Paramagnetic Resonance Linewidth in Cr(III) Complexes

Journal:	<i>Dalton Transactions</i>
Manuscript ID	DT-ART-01-2021-000066.R1
Article Type:	Paper
Date Submitted by the Author:	21-Mar-2021
Complete List of Authors:	<p>Campanella, Anthony; University of Delaware, Chemistry and Biochemistry</p> <p>Nguyen, Manh-Thuong; Pacific Northwest National Laboratory, Catalysis Science</p> <p>Zhang, Jun; Pacific Northwest National Laboratory, Catalysis Science</p> <p>Ngendahimana, Thacien; University of Denver, Chemistry and Biochemistry</p> <p>Antholine, William E.; Medical College of Wisconsin, Department of Biophysics</p> <p>Eaton, Gareth; University of Denver, Chemistry and Biochemistry</p> <p>Eaton, Sandra; University of Denver, Chemistry and Biochemistry</p> <p>Glezakou, Vanda; Pacific Northwest National Laboratory, Catalysis Science</p> <p>Zadrozny, Joseph; Colorado State University, Chemistry</p>

Ligand Control of Low-Frequency Electron Paramagnetic Resonance Linewidth in Cr(III) Complexes

Received 00th January 20xx,
Accepted 00th January 20xx

DOI: 10.1039/x0xx00000x

Anthony J. Campanella,^a Manh-Thuong Nguyen,^b Jun Zhang,^b Thacien Ngendahimana,^c William E. Antholine,^d Gareth R. Eaton,^c Sandra S. Eaton,^c Vassiliki-Alexandra Glezakou,^b and Joseph M. Zadrozny*^a

Understanding how the ligand shell controls low-frequency electron paramagnetic resonance (EPR) spectroscopic properties of metal ions is essential if they are to be used in EPR-based bioimaging schemes. In this work, we probe how specific variations in the ligand structure impact L-band (1–2 GHz) EPR spectroscopic linewidths in the trichloride salts of five Cr(III) complexes [Cr(*RR*-dphen)₃]³⁺ (*RR*-dphen = (1*R*,2*R*)-(+)-diphenylethylenediamine, **1**), [Cr(en)₃]³⁺ (en = ethylenediamine, **2**), [Cr(me-en)₃]³⁺ (me-en = 1,2-diaminopropane, **3**), [Cr(tn)₃]³⁺ (tn = 1,3-diaminopropane, **4**) [Cr(*trans*-chxn)₃]³⁺ (*trans*-chxn = *trans*-(±)-1,2-diaminocyclohexane, **5**). Spectral broadening varies in a nonintuitive manner across the series, showing the sharpest peaks for **1** and broadest for **5**. Molecular dynamics simulations provide evidence that the broadening is correlated to rigidity in the inner coordination sphere and reflected in ligand-dependent distribution of Cr–N bond distances that can be found in frozen solution.

Introduction

Electron paramagnetic resonance imaging (EPRI), the electron spin analogue of nuclear magnetic resonance imaging (colloquially referred to as MRI), could greatly augment the chemical sensing capabilities of MRI.^{1–3} For example, EPRI can track redox status,^{4–7} pH,^{8–11} and oxygenation,^{12–14} thereby delivering local biochemical information that conventional ¹H MRI has considerable difficulty in doing. Merging EPRI with MRI would potentially permit the development of new imaging methodologies that integrate detailed anatomical and chemical information to produce comprehensive physiological maps. However, several key hurdles need to be overcome to mesh EPRI with MRI.

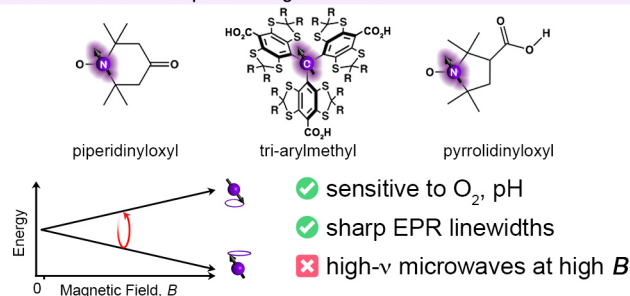
One of the main challenges of merging MRI and EPRI is that EPRI requires microwave radiation. The state-of-the-art EPRI probes are organic radicals with ground state spins of $S = 1/2$.¹ These probes offer sharp linewidths (< 0.1 mT) and long relaxation times ($T_1 \sim 10^{-6}$ s),^{15,16} but require high-frequency microwaves (*ca.* 35 GHz) in a typical MRI magnetic field (1.5 T). Microwaves of this frequency do not efficiently penetrate water-rich tissue and increased microwave power to overcome

this challenge can cause local heating of the biological tissue,^{17–19} thus limiting the utility of these probes in current MRI systems.

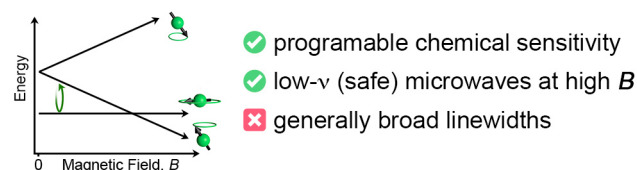
Metal complexes with electronic spins greater than $1/2$ may provide a solution to these challenges. These complexes typically exhibit zero-field splitting (ZFS),^{20,21} which can produce low-frequency EPR transitions at high magnetic fields (Scheme 1). When combined with the widely tunable chemistry of metal ions,²⁰ it becomes clear that they may provide a highly versatile and useful EPRI probe class to develop novel imaging methodologies. To realize this vision, however, we need to understand structure-function relationships for metal complexes and EPR properties at low frequency. This region of

Scheme 1. Overview of EPRI probe classes and advantages.

■ State-of-the-art EPRI probes: Organic Radicals



■ This work: Developing $S > 1/2$ Anisotropic Metal Complexes



^a Department of Chemistry, Colorado State University, Fort Collins, CO 80523, USA. E-mail: joe.zadrozny@colostate.edu

^b Physical Sciences Division, Pacific Northwest National Laboratory, Richland, Washington 99354, USA.

^c Department of Chemistry and Biochemistry, University of Denver, Denver, CO 80208, USA.

^d National Biomedical EPR Center, Medical College of Wisconsin, Milwaukee, WI 53226, USA.

Electronic Supplementary Information (ESI) available: Additional sample preparation details, characterization data, and spectroscopic details. See DOI: 10.1039/x0xx00000x

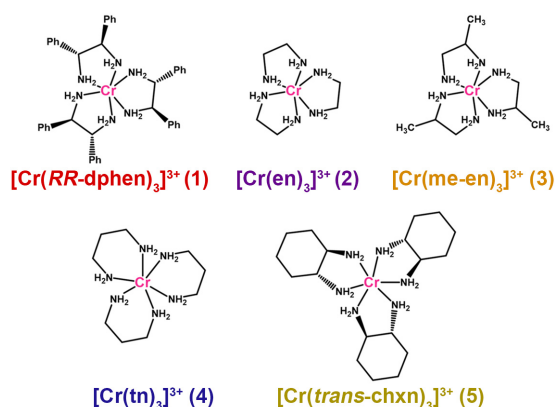


Fig. 1. Bond-line structures of the $S = 3/2$, Cr^{3+} complexes **1-5** used in this study. Cl^- counterions and most hydrogen atoms are omitted for clarity. For complex **1**, the enantiopure (*1R,2R*)-(+)-1,2-diphenylethylenediamine ligand was used and this geometry is depicted. For **5**, the racemic *trans*-(±)-1,2-diaminocyclohexane ligand was used in synthesis. The *R,R* isomer is depicted.

electron spin dynamics is especially under-explored compared to higher frequency/higher field domains, and constitutes a clear “blind spot” in the analysis of metal-ion complexes via magnetic resonance.

A particular challenge to harnessing metal ions for EPRI and related techniques is the extraordinary sensitivity of zero-field splitting to metal ion-electronic structure. A consequence of this sensitivity is a strong inhomogeneous broadening of EPR signals stemming from structural variations in solution.²² In theory, these broad linewidths (typically greater than 1 mT) could prevent spectral resolution of subtle chemical changes. A broad linewidth would also necessitate large magnetic field gradients for the MRI scanner which presents an engineering barrier to implementation. Hence, understanding how to sharpen linewidths by molecular design is a pressing challenge. One path to sharpen linewidths is to install steric bulk in the coordination sphere of a metal ion and hence suppress inhomogeneous broadening due to structural distributions. This tactic is used in manipulating photophysical emission lifetimes^{23–26} but has never been tested for manipulating low-frequency EPR linewidths.

Herein we present the first investigation of the ligand-dependence of the spectral broadening of the L-band (*ca.* 1.3 GHz) EPR spectra of a series of $S = 3/2$ metal complexes. We specifically analyzed a series of Cr(III) *tris*-diamine complexes (Fig. 1) [Cr(*RR*-dphen)₃]₃ (**1**, *RR*-dphen = (*1R,2R*)-(+)-1,2-diphenylethylenediamine), [Cr(en)₃]₃ (**2**, en = ethylenediamine), [Cr(*me-en*)₃]₃ (**3**, *me-en* = 1,2-diaminopropane), [Cr(*tn*)₃]₃ (**4**, *tn* = 1,3-diaminopropane), and [Cr(*trans-chxn*)₃]₃ (**5**, *trans-chxn* = *trans*-(±)-1,2-diaminocyclohexane). In this series, the ligand backbones were selected to test how steric effects in the secondary coordination shell impact EPR linewidth. Our focus here lies on Cr(III) because of the half-integer spin and observable EPR signals for study, as well as the essential potential for low-frequency signals at higher magnetic fields (Fig. 2). We also finally note that this ion

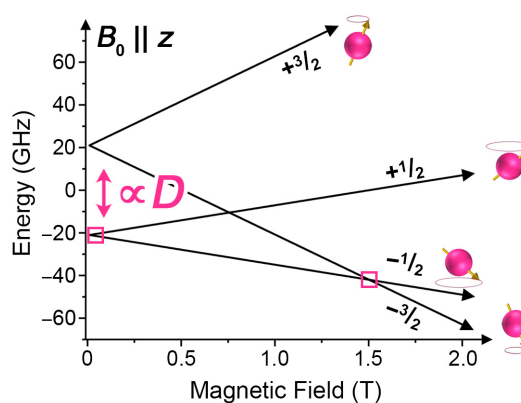


Fig. 2. Calculated M_S -level diagram for an $S = 3/2$ species with positive zero-field splitting ($D = +0.7 \text{ cm}^{-1}$, $g = 2$) and field aligned with the molecular z -axis (approximately the viewing angle in Fig. 1). Potential ground-state low-frequency transitions for these parameters occur near 0.05 T and 1.5 T and are highlighted with small pink boxes.

might be a useful base for a functional agent due to its low toxicity, if an appropriate ligand scaffold were chosen.²⁷

We hypothesized that the systems with the greatest steric congestion in the ligand shell (**1** and **5**) would exhibit the sharpest linewidths. Yet, diamino complexes are known to display multiple structural configurations^{28–30} even when bound to the metal ion. Thus, we envisioned that steric congestion in the ligand scaffold, stemming from intramolecular repulsive interactions between ligand functional groups, would lessen the isomer distribution, consequently sharpening spectra. We did not observe a direct correlation between steric congestion on the ligand shell and EPR spectral sharpness. However, through spectral and molecular dynamics studies, we found that ligand-dependent distributions of Cr–N bond distances appear to correlate to spectral sharpness, underlining a new design strategy for affecting low-frequency EPR linewidths in these and future complexes.

Results and Discussion

Compounds **1-5** were synthesized in a similar manner following a previously reported synthetic pathway of refluxing $\text{CrCl}_3 \cdot 6\text{H}_2\text{O}$ in DMSO, followed by the addition of 3.1 equivalents of the diamine.³¹ In the case of **5**, we prepared two additional isomers of the [Cr(*chxn*)₃]³⁺ complex, using enantiopure ligand starting materials, **5-SS** and **5-RR**. The resulting powders for all syntheses were yellow-orange in color and the UV-visible absorbance spectra matched previous reports.^{31,32}

Surprisingly, the crystal structures of **1**, **4**, **5-SS**, and **5-RR** were unreported at the time of this study, despite the long history of diamine complexes of Cr(III).^{31,33–37} We found that single crystals can be grown via the slow evaporation of a concentrated MeOH solution (**1**) or layering a concentrated aqueous solution with EtOH (**4**, **5-SS**, and **5-RR**) (Fig. 3, Tables 1, S1-S4). Compounds **2** and **5** were identified some time ago.^{38,39}

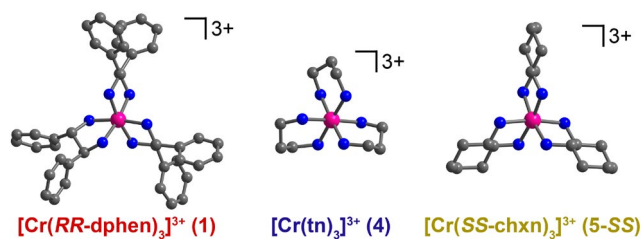


Fig. 3. Molecular structures of $[\text{Cr}(\text{dphen})_3]^{3+}$, $[\text{Cr}(\text{tn})_3]^{3+}$, and $[\text{Cr}(\text{SS-chxn})_3]^{3+}$, as determined in the crystal structures of **1**, **4**, and **5-SS**, respectively. Note that complex **5-SS** contains the enantiopure (1*S*,2*S*)-(+)-1,2-diaminocyclohexane ligand. Pink, blue, and grey spheres represent chromium, nitrogen, and carbon atoms, respectively. Hydrogens and chloride counterions are omitted for clarity. Selected mean interatomic distances and angles can be found in Table 1.

Despite numerous attempts, however, we were unable to grow single crystals of **3** suitable for X-ray diffraction. A summary of structural parameters for **1**, **2**, **4**, and **5** are presented in Table 1. Compound **1** displayed Cr–N bond lengths between 2.057(7) and 2.090(7) Å with bite angles between 80.6(3)° and 82.4(3)°. The M–N lengths found were longer than the 1.968 Å bond lengths seen in the analogous Co(III) complexes.⁴⁰

Complex $[\text{Cr}(\text{tn})_3]^{3+}$ has been structurally characterized with $[\text{Ni}(\text{CN})_5]^{3-}$ and $\text{P}_3\text{O}_9^{3-}$ counterions,^{41–43} but not as the trichloride salt, which we present here. For **4**, we found Cr–N bond lengths ranging between 1.930(17) and 2.35(3) Å with bite angles between 90.3(9)° and 92.2(3)° (average values are given in Table 1). The M–N bond lengths are slightly longer for **4** than **1-3** and **5**, and N–Cr–N bond angles closer to 90° than **1-3** and **5**. Thus, the coordination geometry of **4** more closely resembles an octahedron than the other complexes in this study. These general observations match prior structures^{41–43} and trends in analogous cobalt(III) complexes.^{44–46}

Finally, there does not appear to be substantial difference in bond distances and metrics for the Cr(III) ion in **5-SS** and **5-RR**. These complexes were found to have Cr–N bond lengths between 2.077(5) and 2.085(5) Å for **5-SS**, and between 2.067(5) and 2.084(5) Å for **5-RR**. Bite angles were between 81.7(2)° and 82.4(2)° for **5-SS** and, 82.10(18)° and 82.77(19)° for **5-RR**. The bond distances and angles for these two complexes fall closely in line with those of complex **5**.³⁹

Continuous-Shape-Measurements (CSM) analysis using the SHAPE 2.0 software was performed on all complexes to quantitatively assess any geometric distortions from an idealized geometry.^{47,48} We assessed each complex's geometry relative to those of an idealized octahedron and trigonal prism. A shape measure value, $\underline{S}(\text{O}_h)$, of 0 corresponds to a perfect alignment with an octahedral geometry, whereas an $\underline{S}(\text{O}_h)$, of 16.73 corresponds to a perfect trigonal prismatic geometry. These SHAPE measures for **1**, **2**, **4**, and **5** are in a tight range between 0.064 and 0.731 for an octahedral geometry (O_h) and above 12.00 for the trigonal prismatic geometry (D_{3h}) (Tables 1, S5). These results indicate that the ligands enforce a nearly octahedral environment around the Cr(III) center. Again, no substantial difference was observed between **5-SS** and **5-RR**.

Table 1. Mean structural bond distances (Å), angles (°), and shape-measure analyses from single-crystal diffraction experiments.

	1	2^a	4	5^b
Cr–N	2.075(9)	2.078(17)	2.107(91)	2.079(5)
N–Cr–N _{Bite^c}	81.58(59)	82.66(48)	91.35(72)	82.29(28)
N–Cr–N _{adj^d}	93.0(2.2)	92.58(99)	89.9(4.4)	92.8(1.6)
N–Cr–N _{opp^e}	171(1.4)	173.1(9)	173(2.0)	172(1.1)
$\underline{S}(\text{O}_h)^f$	0.731	0.616	0.064	0.602

^aFrom ref 37. ^bValues computed from averaging **5** (from ref 38), **5-SS**, and **5-RR**. ^cUsing N atoms on the same ligand. ^dAdjacent N atoms of different ligands. ^eBetween N atoms that are *trans* to one another in the coordination shell. ^fShape measure for octahedral geometry: $\underline{S}(\text{O}_h) = 0$ indicates perfect octahedral CrN_6 structure (ref 47).

Continuous-wave (CW) EPR analyses of complexes **1-5** were carried out with L-band (1.3 GHz) and X-band (9.5 GHz) frequencies to directly elucidate spectral linewidths (Figs. 4, S1). The L-band CW-EPR spectra display two notable spectral features for each complex, appearing remarkably similar to X-band spectra for large-zero-field splitting Co(II) complexes.⁴⁹ For **1**, a large $g_{x,y}$ feature is observed at 25 mT and a small, but relatively sharp g_z feature at 50 mT. The basis of these peak assignments is discussed below. From complex **1** to **5**, these features become broader, with the spectrum of **5** much less well-resolved than for **1**. This qualitative trend is mirrored in the data collected at X-band frequency, where the spectra of complexes **1** to **5** were dominated by a sharp feature at 340 mT. While each possessed a large broad feature at 150 mT, this feature decreased in intensity, from very prominent in **1** to nearly unnoticeable in **5**.

EasySpin⁵⁰ was used to simulate the L-band EPR spectra, which enabled the determination of the spin Hamiltonian parameters as well as quantify the spectral broadening in **1-5**. Spectral fits were achieved by simulations using the Spin Hamiltonian: $\hat{H} = g\mu_B\mathbf{B}\hat{S} + \hat{S}\mathbf{D}\hat{S}$. Here, g is an axial g -factor ($g_x = g_y \neq g_z$), μ_B is the Bohr magneton, \mathbf{B} is the external applied magnetic field, \hat{S} is the electronic spin, and \mathbf{D} is the axial zero field splitting term. Since Cr has only a 9.5% natural abundance in the $I = 1/2$ ⁵³Cr isotope,⁵¹ hyperfine interactions (usually denoted with \mathbf{A}) between the $S = 3/2$ spin and the nuclear spin were neglected. To account for the observed spectral broadening, we employed a model that explicitly averaged simulated spectra over a distribution of g_z and $g_{x,y}$ values. This model is relatively uncommon compared to typically applied isotropic broadening models or strains.^{50,52}

As depicted in Figs. 4 and S13, the broadening model and spin Hamiltonian permitted high-quality simulations of the L-band spectra for **1-5**. The determined g values for **1-5** are generally axial with $g_{x,y} > g_z$. The $g_{x,y}$ for **3** is the smallest of the series (1.985) and greatest for **4** and **5** (2.300). Across **1-5**, g_z varies significantly less, from 1.955 for **1** to 2.000 for **5**. The determined D values were all positive and *ca.* 3 GHz (roughly 0.1 cm^{-1}) for all complexes: 3.2(7), 3.0(3), 2.8(3), 2.9(7), and 2.9(4) GHz, for **1-5**, respectively (0.11(2), 0.10(1), 0.09(1), 0.09(2), and 0.09(1) cm^{-1} for **1-5** respectively). Here, errors are estimated by eye from inspection of simulation quality upon variation of D ,

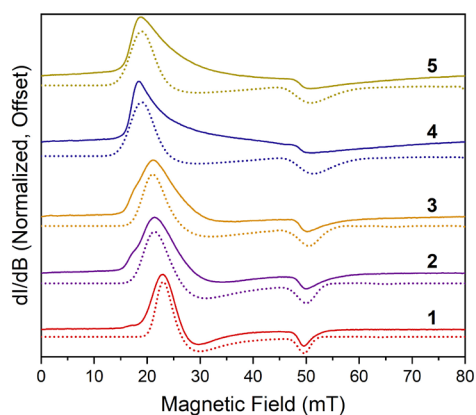


Fig. 4. L-band (1.359 GHz) continuous wave EPR spectra for **1-5** in frozen glass solutions. Compounds were dissolved at 30 mM concentration in an ethylene glycol/water (1:1 v/v) solvent system and data collected at 112 K. Modulation amplitude was 0.8 mT, modulation frequency was 100 kHz, non-saturating power was used, and gain was 4×10^3 dB. Dotted lines are simulations that treat broadening with a distribution of g values, see main text for details.

since Easyspin does not determine uncertainties. Importantly, these g and D values are similar in magnitude and sign to prior analyses of Cr^{3+} diamine complexes.⁵³⁻⁵⁶ Note that simulation quality was not improved by the inclusion of E though this parameter (while small relative to D) is expected to be present.⁵⁷⁻⁶¹ A full list of the parameters determined by the best simulations of each spectrum are tabulated in Table S11.

The spin Hamiltonian parameters from the simulations give insight into the nature of the observed transitions in the L-band spectrum (Fig. 5). The low-field transition involves levels of mixed identity that are mostly $M_S = \pm 1/2$ character, but with a significant (*ca.* 8 %) $M_S = \pm 3/2$ component, and stems from Cr^{3+} molecules aligned perpendicular to the applied magnetic field, B_0 . The high-field transition (near 50 mT), in contrast, stems from molecules aligned parallel to B_0 , and is a transition between unmixed $M_S = \pm 1/2$ levels. Finally, the spin Hamiltonian values predict low-frequency transitions at fields beyond the range of the used instrument. For example, for **1**, crossing of the $M_S = -3/2$ and $M_S = -1/2$ levels at 237 mT means that EPR transitions below 1 GHz are possible within the 200 to 273 mT window.

The broadening model provides a direct way to quantitate the trend in spectral shape shown in Fig. 4. Here, the changing signal shape from two resolved peaks in the first-derivative spectrum to the broadened signal can be quantified with the full width at half maximum (FWHM) of the distribution of each g value for **1-5**. For the L-band spectra, the g_z FWHM values are 0.01, 0.1, 0.8, 0.38, and 0.4, respectively, for **1-5**, generally increasing across the probed molecules (with **3** as the exception). For $g_{x,y}$, the FWHM of the parameter is considerably larger than g_z for all studied complexes. Indeed, the FWHM for $g_{x,y}$ varies, respectively, as 0.6, 0.8, 1.12, 3.80, and 4.0 for **1-5**. From these data, it appears that the broadening of $g_{x,y}$ is the most important feature in dictating the spectral shape, as it is this g factor that directly affects the energy of the low-field

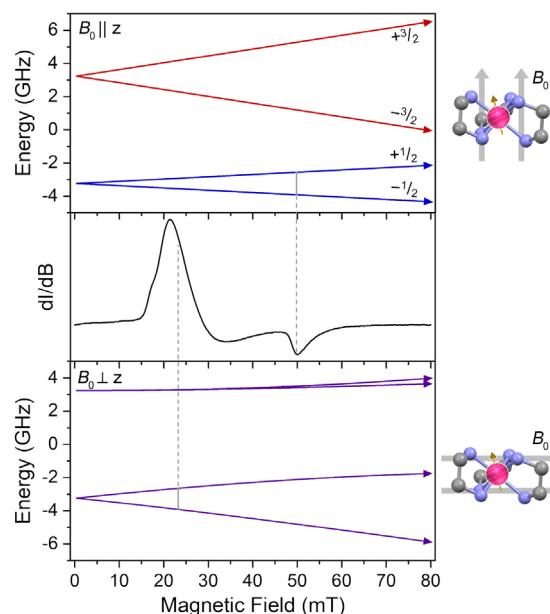


Fig. 5. Spectral assignment for L-band EPR spectrum of **2**. The top- and bottom-most panels are M_S -level energies computed for B_0 parallel and perpendicular to the molecular C_3 axis, respectively. M_S -level energies were calculated with $g_{x,y} = 1.985$; $g_z = 1.960$; $D = +0.1 \text{ cm}^{-1}$, $E = 0 \text{ cm}^{-1}$. Dashed lines correlate peaks to indicated transitions between levels. Energies and level compositions were computed with Easyspin,⁵⁰ see main text for details.

transition in Fig. 5. Thus, these analyses suggest that the broadening of $g_{x,y}$ (and hence the low-field transition) is responsible for the trend in spectral shape.

On the basis of a superficial prediction of sharper linewidths from steric bulk on ligands, **1** and **5** were expected to yield the sharpest peaks. Instead, these ligands produced the sharpest (**1**) and broadest (**5**) spectra. Hence, we sought a more quantitative estimate of rigidity in the coordination shell of the Cr^{3+} metal ion. Tests of correlation between rigidity and ligand identity were pursued in a three-fold manner: by electronic absorption/emission spectroscopies, ligand isomer identity, and then, finally, molecular dynamics simulations.

Steady-state and time-resolved photoemission analyses of **1-5** were carried out as the first measure of quantifying rigidity in the ligand shell. Indeed, intense, long-lived emission is a sign of a rigid environment.^{23,24,62} Complexes **1-5** are all emissive. Analyses of 30 mM aqueous solution of **1-5** with 460 nm excitation revealed a prominent emission generally near 675 nm (Figure S8). The shape and intensity of this emission peak varied, with **1**, **2**, and **5** having a relatively intense single peak, while **3** and **4** exhibited smaller peaks. The luminescence decays of these peaks were collected (Figures S10-S11) to provide the time constants of the decays (Table S10), which can serve as a quantitative measure for molecular rigidity.²³⁻²⁶ The time-resolved emission data for **1-5** were best fit using either a bi- (**2-5**) or tri-exponential (**1**) decay model. Complexes **2-5** exhibit two starkly different relaxation emission decay times (τ): the first (τ_1) was on the order of 1 ns, and the second (τ_2) was on the order of 2 μs . Studies on similarly structured $\text{Cr}(\text{III})$ hexamine

complexes indicate that the faster τ_1 corresponds to fluorescence, while τ_2 corresponds to a longer-lived phosphorescence.⁶³ For complex **1**, the tri-exponential decay yielded three lifetimes, $\tau_1 = 0.45(3)$, $\tau_2 = 38(5)$, and $\tau_3 = 1884(66)$ ns. Note that the free ligand (1*R*,2*R*)-(+)-1,2-diphenylethylenediamine in aqueous solution has an emission lifetime on the same order as τ_1 for **1** (Fig. S12).⁶⁴ Hence we can conclude that the τ_2 from complex **1** is likely ligand-related, and τ_3 is metal-ion phosphorescence.

More importantly, our analysis suggests that emission as an indicator of rigidity appears to fail in describing the EPR broadening. Indeed, by the metric of the emission lifetimes, **2** is the most rigid complex with $\tau_1 = 1.40(5)$ ns, followed by **3** ($\tau_1 = 0.99(5)$ ns), **5** ($\tau_1 = 0.97(6)$ ns), **4** ($\tau_1 = 0.48(6)$ ns), and **1** ($\tau_1 = 0.45(3)$ ns). This ordering of rigidity does not correlate with the observed trend of **1** < **2** < **3** < **4** < **5** in the FWHM of g_{xy} . Emission lifetimes and rigidity can frequently be correlated directly with specific structural features, e.g. C–H v. C–D functionalization.⁶⁵ Thus, this work suggests that, at least for **1**-**5**, and possibly for other open-shell complexes, the specific “rigid” structural features that impact photophysics and EPR linewidth are not entirely coincident.

Our second and third tests of rigidity probed direct structural factors. First, note that *tris*-bidentate metal complexes exhibit stereochemistry that is influenced by the identity of the ligand backbone. Indeed, several previous studies of analogous *tris*-diamine metal complexes demonstrate that there are myriad isomers possible.^{66,67} To test if the number of isomers influences EPR spectral linewidth, as these may each impose different g or D values (and thus broaden the signals), we synthesized and analysed **5-SS**, a chemically identical complex to **5**, but using the enantiopure (1*S*,2*S*)-(+)-1,2-diaminocyclohexane, instead of racemic *trans*-(±)-1,2-diaminocyclohexane. The use of this ligand reduced the number of possible isomers from eight to two. We hypothesized that we would observe a sharper spectrum for complex **5-SS** compared to **5**, if the number of isomers dictates spectral broadness in this system.

Continuous-wave L-band EPR spectra were collected for **5-SS** in identical sample conditions to **5** and was subsequently modelled with EasySpin⁵⁰ to extract the spin Hamiltonian parameters (Fig. S13, Table S11). There is a field offset because of differing experiment frequencies (1.360 GHz for **5** and 1.095 GHz for **5-SS**). However, adequate simulations of both spectra could be achieved using the same simulation parameters. Furthermore, the FWHM of the g_{xy} term was the same (4.0) in the analysis. This result indicates that EPR line broadening is likely not influenced by the number of isomers of a given species, and thus the differences in the possible number of isomers between **1**-**5** likely is not responsible for the observed trend in linewidth.

Systems **1**, **2**, **4**, and **5**, for which crystal structures are available in this work or others,^{38,39} were further investigated by means of quantum chemical (QC) calculations and *ab initio* molecular dynamics (AIMD) simulations in explicit water (Fig. 6). The purpose of these simulations is to test for correlations between mean atomic displacements in the first coordination

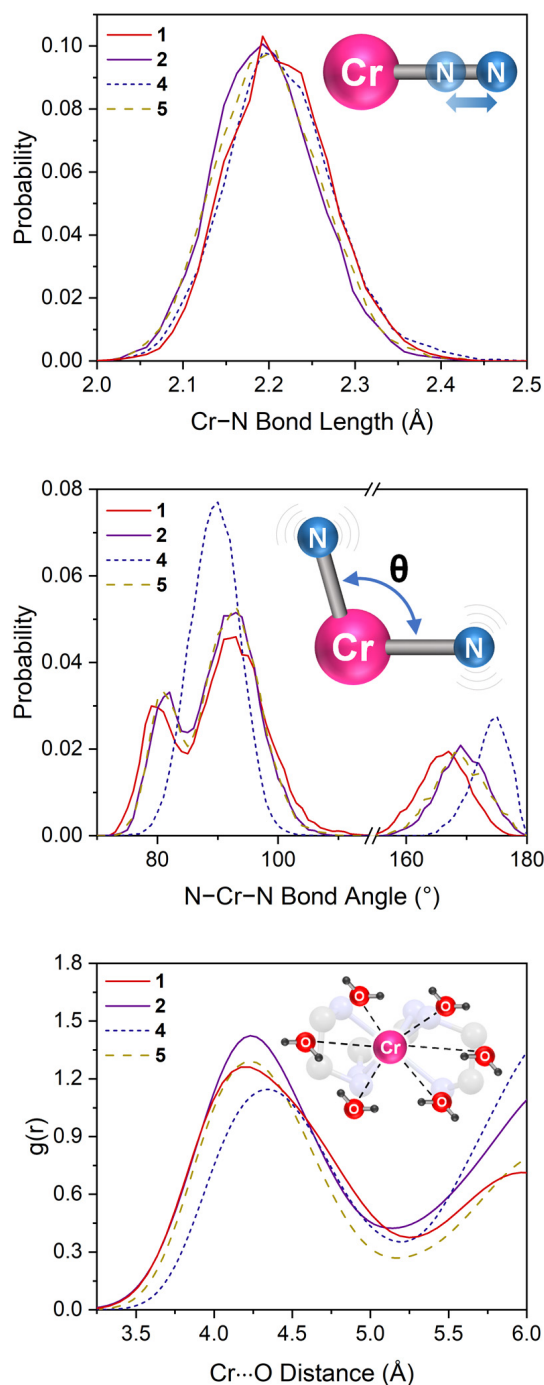


Fig. 6. Top: Simulated distribution of Cr–N bond lengths for complexes **1**, **2**, **4**, and **5**. Middle: Simulated distribution of N–Cr–N bond angles for complexes **1**, **2**, **4**, and **5**. Bottom: Simulated distribution of distances between Cr(III) metal centres and the oxygen atoms of surrounding water molecules for complexes **1**, **2**, **4**, and **5**. See main text and ESI for computational details.

shell (as a function of ligand) and the EPR spectral shape. The structures of **1**, **2**, **4**, and **5** micro-solvated by 20 water molecules were first optimized at the TPSSH+D3BJ/def2-TZVP level of theory using NWPEsE (Fig. S14).⁶⁸ The optimized structures were then used as initial structures in the following

Table 2. Mean structural bond distances (Å) and angles (°) from QC^a calculations and AIMD^b simulations.

	1	2	4	5
Cr–N (QC)	2.102	2.125	2.134	2.116
Cr–N (AIMD)	2.213	2.197	2.214	2.200
FWHM	0.120	0.118	0.128	0.123
N–Cr–N _{Bite} (QC)	80.7	80.9	89.5	80.9
N–Cr–N _{Bite} (AIMD)	79.8	81.0	89.4	80.9
N–Cr–N _{adj} (QC)	93.1	94.0	90.1	93.8
N–Cr–N _{adj} (AIMD)	93.2	92.6	89.5	92.6
N–Cr–N _{opp} (QC)	171.3	170.9	178.6	170.6
N–Cr–N _{opp} (AIMD)	166.2	169.2	173.8	168.9

^aQC = Quantum chemical. ^bAIMD = Ab initio molecular dynamics

AIMD simulations in water boxes (Fig. S15). Relevant structural parameters are listed in Table 2.

Molecular dynamics (MD) simulations are commonly used for simulating EPR spectra in spin-labelled proteins,^{69–71} or evaluating distances between metal complexes (either as spin labels⁷² or aggregates⁷³). Here we present, to the best of our knowledge, the first effort to use MD simulations to understand EPR spectral linewidth of $S > 1/2$ metal complexes. Note that the following structural analyses from AIMD simulations are obtained from solution-phase environments. These conditions are different than the frozen-glass solutions that produced the spectra in Figs. 4 and 5. In the following analysis and discussion, we consider the spectra of the frozen glasses to provide a “snapshot” of the distribution of possible geometries of the Cr³⁺ complexes in solution when frozen.

AIMD simulations were conducted using the CP2K package.⁷⁴ The potential energy surface was calculated at the PBE-D3 density functional⁷⁵ level of theory with Grimmes' correction for dispersion.⁷⁶ We adopted the Gaussian-Plane wave hybrid basis set scheme,⁷⁷ in which the Gaussian basis sets of the DVZP quality, in conjunction with a plane wave energy cut-off of 450 Ry, were used. MD simulations were performed within the NVT ensemble, with the temperature kept at 300 K with a velocity-rescaling thermostat.⁷⁸ For each simulation of a complex, the Cr(III) complex, three Cl⁻ counterions, and a box of water solvent molecules were initially equilibrated for at least 8 ps, followed with 10 ps production runs that were finally used for the computation of properties. Additional details for the simulations can be found in the ESI.

The structural parameters deduced from the AIMD simulations exhibit distributions in structural metrics, but are otherwise similar to the crystalline structures. For example, all complexes are six-coordinate throughout the 10 ps time window, and distributions in observed Cr–N bond distances are all centered around 2.2 Å (Fig. 6), which is close to the crystal structures. We note, however, that the full widths at half maxima of the Cr–N distributions change with the ligand: 0.120 Å for **1**, 0.118 Å for **2**, 0.128 Å for **4**, and 0.123 Å for **5**. The simulations also reveal that all complexes exhibit distributions in N–Cr–N angles (Fig. 6), also close to the crystal structures.^{38,39} For example, for **1**, **2**, and **5**, three peaks are exhibited in the

distributions at ca. 79° (bite angle), 94° (adjacent N atoms on different ligands), and 170° (approximately *trans* N atoms). Complex **4**, in contrast, exhibits only two peaks, one near 90° and one closer to 175°. Here, the sharpest two angles are relatively close in value, potentially encouraged by ligand strain, and consistent with solution-phase extended x-ray absorption fine-structure analyses of [Co(tn)₃]³⁺.⁷⁹ We note that perfect agreement should not be expected for any structural parameter here since the crystalline environment is more rigid than the fluxional one in solution captured by molecular dynamics simulations.

The simulations also provided insights into the solvation structure of the complexes, by revealing the radial distribution function, $g(r)$, that provides a measure of the average M•••O_{water} distance and its fluctuation over the simulation period. For **1**, **2**, **4**, and **5**, the computed $g(r)$ places the first solvent shell near 4.2 Å for all complexes: 4.17 Å for **1**, 4.23 Å for **2**, 4.34 Å for **4**, and 4.23 Å for **5**. Beyond 5 Å, a rise in $g(r)$ is observed for all complexes, indicating the start of the second solvent shell in the 5.5–5.75 Å range.

The distributions of bond angles, bond distances, and solvent shell values were compared with the observed spectroscopic trends. We reasoned that the relative rigidity in the coordination shell correlates with the relatively tighter distributions of observed bond distances and angles from the 10 ps trajectory in solution for **1**, **2**, **4**, and **5**. The one parameter that approximately correlates to the observed spectral trend is the distribution in Cr–N bond distances. Complexes **1** and **2** have relatively sharper EPR spectra, smaller g_{xy} FWHM values, and slightly sharper distributions in the simulated Cr–N distances. Complexes **4** and **5**, in contrast, have slightly larger Cr–N distributions, which would broaden spectra by producing variation in electronic structure.^{80,81} We tentatively speculate that **4** and **5** produce both broader distributions and spectra owing to more efficient structural trans-effect interactions between the N donor atoms. This effect results in larger M–L bond distances for donor atoms that are directly *trans* to another atom, which has been observed with larger mean atomic displacements in crystal structures of other metal complexes.^{82,83} Indeed, **4** and **5** are closest to O_h geometry (from the SHAPE measure analysis). Thus, the N–Cr–N bond angles between *trans* N-donors in **4** and **5** are overall closer to 180°, enabling a stronger structural trans effect. If true, this idea suggests that geometries where the trans-effect is less operative (e.g. T_d or perhaps trigonal-prismatic coordination) are particularly promising for future molecules with sharper linewidths. Finally, we note that the observed difference between the distributions of **1**, **2**, **4**, and **5** is small, suggesting an extremely high sensitivity of spectral shape to ligand field.

Our calculations suggest variability in Cr–N bond lengths of over 0.2 Å (~10% based on *total* width of the distributions), which we infer leads to a large variation of g -values. We also suggest that the relative changes in the FWHM of these distributions, while small (e.g. 0.003 Å between **1** and **5**), are appreciably affecting relative linewidth. For this last point, literature evidence supports that relatively tiny changes can induce large changes to EPR spectra. For example, variable-

pressure studies of Cr-doped solids ($\text{Al}_2\text{O}_3\text{:Cr}$ and $\text{Al}_2(\text{SO}_4)_3\text{:Cr}$) show pressure dependence of zero-field splitting^{84,85} and g -values⁸⁵, in some cases showing *ca.* 0.005 changes in g with 0.02 Å changes in Cr–O bond distances.^{85,86} In a 1 GHz EPR spectrum at $g = 2.00$, a variation in g of ± 0.15 would induce a 60 G span for the EPR peak, well within the width of the full spectra shown in Fig. 4. Thus, these data suggest that the ligand-based distributions in observed Cr–N bond distances are affecting spectral shape, though quantitative correlation will likely need deeper studies of solution structure (e.g. by extended X-ray absorption fine structure spectroscopy), which are underway.

Conclusions

The foregoing study is the first analysis of low-frequency EPR linewidth as a function of ligand identity in $S > 1/2$ metal complexes. Most importantly, our studies of *tris*-diamine Cr^{3+} complexes reveal three novel insights:

(i) Relatively minor changes in ligand identity can impact the L-band EPR spectral shape, which has important implications for, e.g., using tuneable ligand fields to image local chemistry via magnetic resonance.

(ii) Our studies show that the same parameters that define “rigidity” in the sense of photochemical lifetimes do not correlate to EPR linewidth, suggesting more detailed approaches to rigidity design are necessary in this new field.

(iii) Finally, our studies suggest that EPR linewidth in Cr^{3+} complexes can be correlated to variation in Cr–L bond distance variation in frozen solution.

This final outcome suggests that many tuneable aspects of metal complexes, e.g. donor atom, metal-ligand bond strength, and covalency, can all be harnessed to manipulate low-frequency EPR linewidth by controlling metal-ligand interactions. We note that the linewidths here (> 10 G) are still substantially larger than organic radicals under similar conditions (< 1 G).¹⁵ Thus, further tests of the effects of ligand shells on linewidth are clearly needed for functional metal-ion based EPRI molecular probes. Such studies are ongoing and will be reported in the near future.

Conflicts of interest

There are no conflicts to declare.

Acknowledgements

We thank Prof. M. Reynolds, C. Allison, and M. Roach for use of their mass spectrometer. This research was performed with the support of Colorado State University (CSU) and the NIH (R21-EB027293) (A.J.C., J.M.Z.). Part of the work described in this publication was performed at Pacific Northwest National Laboratory (PNNL), which is operated by Battelle for the United States Department of Energy (DOE) under Contract DE - AC05 - 76RL01830. M.-T.N., J.Z. and V.-A.G. acknowledge support from the U.S. Department of Energy, Office of Science, Office of Basic Energy Sciences, Division of Chemical Sciences,

Geosciences, and Biosciences. Computational resources were provided by the National Energy Research Scientific Computing Center (NERSC), a U.S. Department of Energy Office of Science User Facility operated under Contract No. DE - AC02 - 05CH11231 and PNNL's Research Computing.

Notes and references

- 1 L. J. Berliner, Ed., *In Vivo EPR (ESR): Theory and Application*, Springer US, 2003.
- 2 J. P. Klare, *Biomed. Spectrosc. Imaging*, 2012, 101–124.
- 3 S. Colacicchi, M. Ferrari and A. Sotgiu, *Int. J. Biochem.*, 1992, **24**, 205–214.
- 4 G. L. Caia, O. V. Efimova, M. Velayutham, M. A. El-Mahdy, T. M. Abdelghany, E. Kesselring, S. Petryakov, Z. Sun, A. Samouilov and J. L. Zweier, *J. Magn. Reson.*, 2012, **216**, 21–27.
- 5 T. Mikuni, G. He, S. Petryakov, M. M. Fallouh, Y. Deng, R. Ishihara, P. Kuppusamy, M. Tatsuta and J. L. Zweier, *Cancer Res.*, 2004, **64**, 6495–6502.
- 6 F. Hyodo, R. Murugesan, K. Matsumoto, E. Hyodo, S. Subramanian, J. B. Mitchell and M. C. Krishna, *J. Magn. Reson.*, 2008, **190**, 105–112.
- 7 B. Epel, S. V. Sundramoorthy, M. Krzykowska-Serda, M. C. Maggio, M. Tseytlin, G. R. Eaton, S. S. Eaton, G. M. Rosen, J. P. Y. Kao and H. J. Halpern, *J. Magn. Reson.* 2017, **276**, 31–36.
- 8 M. A. Voinov, J. F. Polienko, T. Schanding, A. A. Bobko, V. V. Khramtsov, Y. V. Gatilov, T. V. Rybalova, A. I. Smirnov and I. A. Grigor'ev, *J. Org. Chem.*, 2005, **70**, 9702–9711.
- 9 M. A. Voinov, C. T. Scheid, I. A. Kirilyuk, D. G. Trofimov and A. I. Smirnov, *J. Phys. Chem. B*, 2017, **121**, 2443–2453.
- 10 B. Gallez, K. Mader and H. M. Swartz, *Magn. Reson. Med.*, 1996, **36**, 694–697.
- 11 D. I. Potapenko, M. A. Foster, D. J. Lurie, I. A. Kirilyuk, J. M. S. Hutchison, I. A. Grigor'ev, E. G. Bagryanskaya and V. V. Khramtsov, *J. Magn. Reson.*, 2006, **182**, 1–11.
- 12 Gareth R. Eaton, Sandra S. Eaton, and Keiichi Ohno, Eds., *EPR Imaging and in Vivo EPR*, CRC Press, 1991.
- 13 F. Demsar, T. Walczak, P. D. Morse, G. Bačić, Z. Zolnai and H. M. Swartz, *J. Magn. Reson.*, 1988, **76**, 224–231.
- 14 H. M. Swartz, A. B. Flood, P. E. Schaner, H. Halpern, B. B. Williams, B. W. Pogue, B. Gallez and P. Vaupel, *Physiol. Rep.*, 2020, **8**, e14541.
- 15 S. R. Burks, M. A. Makowsky, Z. A. Yaffe, C. Hoggle, P. Tsai, S. Muralidharan, M. K. Bowman, J. P. Y. Kao and G. M. Rosen, *J. Org. Chem.*, 2010, **75**, 4737–4741.
- 16 J. R. Biller, V. Meyer, H. Elajaili, G. M. Rosen, J. P. Y. Kao, S. S. Eaton and G. R. Eaton, *J. Magn. Reson.*, 2011, **212**, 370–377.
- 17 R. T. Hitchcock, *Radio-frequency and Microwave Radiation*, AIHA, 2004.
- 18 J. Fuchs, T. Herrling and N. Groth, in *Current Problems in Dermatology*, eds. J. Thiele and P. Elsner, KARGER, Basel, 2000, vol. 29, pp. 1–17.
- 19 P. Danhier and B. Gallez, *Contrast Media Mol. Imaging*, 2015, **10**, 266–281.
- 20 J. S. Griffith, *The Theory of Transition-Metal Ions*, Cambridge University Press, 1964.
- 21 B. N. Figgis and M. A. Hitchman, *Ligand field theory and its applications*, Wiley-VCH, 2000.
- 22 C. P. Poole and H. A. Farach, *Bull. Magn. Reson.*, 1979, **1**, 162–194.

- 23 M. K. DeArmond, *Acc. Chem. Res.*, 1974, **7**, 309–315.
- 24 D. M. Roundhill, *Photochemistry and Photophysics of Metal Complexes*, Springer US, 1994.
- 25 A. F. Rausch, L. Murphy, J. A. G. Williams and H. Yersin, *Inorg. Chem.*, 2012, **51**, 312–319.
- 26 G. Li, F. Zhan, J. Zheng, Y.-F. Yang, Q. Wang, Q. Chen, G. Shen and Y. She, *Inorg. Chem.*, 2020, **59**, 3718–3729.
- 27 J. B. Vincent and H. C. Lukaski, *Adv. Nutr.*, 2018, **9**, 505–506.
- 28 Z. D. Matović, A. Meetsma, V. D. Miletić and P. J. van Koningsbruggen, *Inorg. Chim. Acta*, 2007, **360**, 2420–2431.
- 29 S. Belošević, M. Ćendić, M. Djukić, M. Vasojević, A. Meetsma and Z. D. Matović, *Inorganica Chim. Acta*, 2013, **399**, 146–153.
- 30 R. Noyori, *Angew. Chem. Int. Ed.*, 2002, **41**, 2008–2022.
- 31 E. Pedersen, *Acta Chem. Scand.*, 1970, **24**, 3362–3372.
- 32 R. D. Gillard, P. R. Mitchell, D. H. Busch, C. R. Sperati, H. B. Jonassen and C. W. Weston, *Inorg. Synth.*, 2007, **38**, 184–186.
- 33 S. R. Niketic, K. Rasmussen, F. Woldbye, S. Lifson and J. Koskikallio, *Acta Chem. Scand.*, 1976, **30a**, 485–497.
- 34 H. Toftlund and E. Pedersen, *Acta Chem. Scand.*, 1972, **26**, 4019–4030.
- 35 J. L. Bear and W. W. Wendlandt, *J. Inorg. Nucl. Chem.*, 1961, **17**, 286–294.
- 36 P. Pfeiffer and M. Haimann, *Ber. Dtsch. Chem. Ges.*, 1903, **36**, 1063–1069.
- 37 P. Pfeiffer, *Z. Für Anorg. Chem.*, 1900, **24**, 279–304.
- 38 A. Whuler, C. Brouty, P. Spinat and P. Herpin, *Acta Crystallogr. Sect. B*, 1977, **33**, 2877–2885.
- 39 I. Kalf, B. Calmuschi and U. Englert, *CrystEngComm*, 2002, **4**, 548–551.
- 40 K. G. Lewis, S. K. Ghosh, N. Bhuvanesh and J. A. Gladysz, *ACS Cent. Sci.*, 2015, **1**, 50–56.
- 41 T. G. Spiro, A. Terzis and K. N. Raymond, *Inorg. Chem.*, 1970, **9**, 2415–2420.
- 42 F. A. Jurnak and K. N. Raymond, *Inorg. Chem.*, 1974, **13**, 2387–2397.
- 43 Y. Sunatsuki, S. Miyahara, T. Suzuki, M. Kojima, T. Nakashima, N. Matsumoto and F. Galsbøl, *New J. Chem.*, 2010, **34**, 2777–2784.
- 44 R. Nagao, F. Marumo and Y. Saito, *Acta Crystallogr. B*, 1973, **29**, 2438–2443.
- 45 Y. Saito, H. Iwasaki and H. Ota, *Bull. Chem. Soc. Jpn.*, 1963, **36**, 1543–1544.
- 46 T. Nomura, F. Marumo and Y. Saito, *Bull. Chem. Soc. Jpn.*, 1969, **42**, 1016–1020.
- 47 S. Alvarez, D. Avnir, M. Llundell and M. Pinsky, *New J. Chem.*, 2002, **26**, 996–1009.
- 48 S. Alvarez, P. Alemany, D. Casanova, J. Cirera, M. Llundell and D. Avnir, *Coord. Chem. Rev.*, 2005, **249**, 1693–1708.
- 49 A. R. Marts, S. M. Greer, D. R. Whitehead, T. M. Woodruff, R. M. Breece, S. W. Shim, S. N. Oseback, E. T. Papish, F. E. Jacobsen, S. M. Cohen and D. L. Tierney, *Appl. Magn. Reson.*, 2011, **40**, 501–511.
- 50 S. Stoll and A. Schweiger, *J. Magn. Reson.*, 2006, **178**, 42–55.
- 51 D. R. Lide, Ed., *CRC Handbook of Chemistry and Physics*, CRC Press, Boca Raton, FL, 85th edn., 2004.
- 52 W. Froncisz and J. S. Hyde, *J. Chem. Phys.*, 1980, **73**, 3123–3131.
- 53 R. P. Bonomo and A. J. Di Bilio, *Chem. Phys.*, 1991, **151**, 323–333.
- 54 B. R. McGarvey, *J. Chem. Phys.*, 1964, **41**, 3743–3758.
- 55 B. R. McGarvey, *J. Chem. Phys.*, 1962, **37**, 3020–3021.
- 56 J. C. Hempel, L. O. Morgan and W. B. Lewis, *Inorg. Chem.*, 1970, **9**, 2064–2072.
- 57 M. Açıkgöz, *J. Phys. Chem. Solids*, 2016, **98**, 115–122.
- 58 M. Açıkgöz, *J. Fluor. Chem.*, 2015, **175**, 152–159.
- 59 D. Žilić, L. Androš Dubraja, Y. Krupskaya, V. Kataev and B. Büchner, *Appl. Magn. Reson.*, 2015, **46**, 309–321.
- 60 R. Kripal and A. K. Yadav, *Chem. Phys. Lett.*, 2014, **612**, 245–250.
- 61 K. H. Zangana, E. M. Pineda, I. J. Vitorica-Yrezabal, E. J. L. McInnes and R. E. P. Winpenny, *Dalton Trans.*, 2014, **43**, 13242–13249.
- 62 D. Su, C. L. Teoh, L. Wang, X. Liu and Y.-T. Chang, *Chem. Soc. Rev.*, 2017, **46**, 4833–4844.
- 63 P. Comba, A. W. H. Mau and A. M. Sargeson, *J. Phys. Chem.*, 1985, **89**, 394–396.
- 64 A. Santoro, L. J. Kershaw Cook, R. Kulmaczewski, S. A. Barrett, O. Cespedes and M. A. Halcrow, *Inorg. Chem.*, 2015, **54**, 682–693.
- 65 G. A. Hebbink, D. N. Reinhoudt and F. C. J. M. van Veggel, *Eur. J. Org. Chem.*, 2001, **2001**, 4101–4106.
- 66 A. Ehnborn, S. K. Ghosh, K. G. Lewis and J. A. Gladysz, *Chem. Soc. Rev.*, 2016, **45**, 6799–6811.
- 67 F. A. Jurnak and K. N. Raymond, *Inorg. Chem.*, 1972, **11**, 3149–3152.
- 68 J. Zhang, V.-A. Glezakou, R. Rousseau and M.-T. Nguyen, *J. Chem. Theory Comput.*, 2020, **16**, 3947–3958.
- 69 Y.-W. Huang and Y.-W. Chiang, *Phys. Chem. Chem. Phys.*, 2011, **13**, 17521–17531.
- 70 P. D. Martin, B. Svensson, D. D. Thomas and S. Stoll, *J. Phys. Chem. B*, 2019, **123**, 10131–10141.
- 71 G. Jeschke, *Annu. Rev. Phys. Chem.*, 2012, **63**, 419–446.
- 72 A. Gamble Jarvi, A. Sargun, X. Bogetti, J. Wang, C. Achim and S. Saxena, *J. Phys. Chem. B*, 2020, **124**, 7544–7556.
- 73 S. J. Lockyer, S. Nawaz, A. Brookfield, A. J. Fielding, I. J. Vitorica-Yrezabal, G. A. Timco, N. A. Burton, A. M. Bowen, R. E. P. Winpenny and E. J. L. McInnes, *J. Am. Chem. Soc.*, 2020, **142**, 15941–15949.
- 74 J. Hutter, M. Iannuzzi, F. Schiffmann and J. VandeVondele, *WIREs Comput. Mol. Sci.*, 2014, **4**, 15–25.
- 75 J. P. Perdew, K. Burke and M. Ernzerhof, *Phys. Rev. Lett.*, 1996, **77**, 3865–3868.
- 76 S. Grimme, J. Antony, S. Ehrlich and H. Krieg, *J. Chem. Phys.*, 2010, **132**, 154104.
- 77 G. Lippert, J. Hutter and M. Parrinello, *Mol. Phys.*, 1997, **92**, 477–488.
- 78 G. Bussi, D. Donadio and M. Parrinello, *J. Chem. Phys.*, 2007, **126**, 014101.
- 79 T. M. Ozvat, G. E. Sterbinsky, A. J. Campanella, A. K. Rappé and J. M. Zadrozny, *Dalton Trans.*, 2020, **49**, 16380–16385.
- 80 A. Abragam and B. Bleaney, *Electron Paramagnetic Resonance of Transition Ions*, OUP Oxford, 2012.
- 81 D. Dai, H. Xiang and M.-H. Whangbo, *J. Comput. Chem.*, 2008, **29**, 2187–2209.
- 82 B. J. Coe and S. J. Glenwright, *Coord. Chem. Rev.*, 2000, **203**, 5–80.
- 83 R. C. Elder, M. J. Heeg, M. D. Payne, M. Trkula and E. Deutsch, *Inorg. Chem.*, 1978, **17**, 431–440.
- 84 K. Bielecki, *Phys. Status Solidi B*, 1988, **148**, K53–K56.
- 85 H. M. Nelson, D. B. Larson and J. H. Gardner, *J. Chem. Phys.*, 1967, **47**, 1994–1998.
- 86 L. W. Finger and R. M. Hazen, *J. Appl. Phys.*, 1978, **49**, 5823–5826.